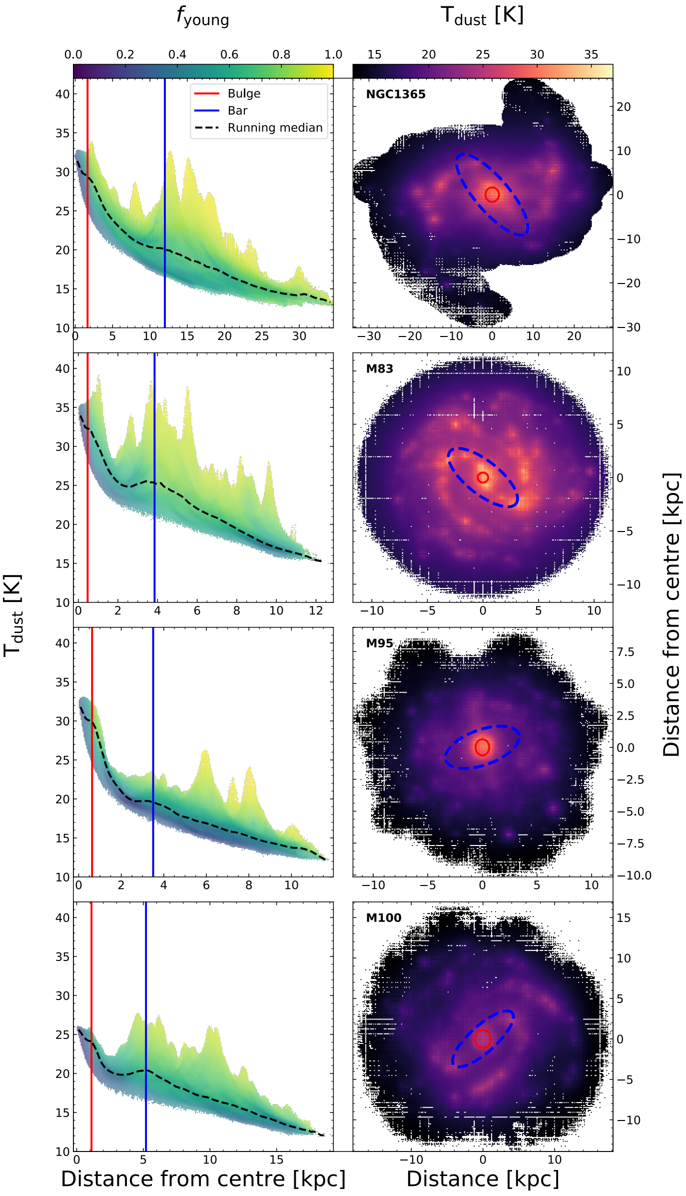

Fig. 9. *Left column*: distribution of the temperature of the diffuse dust with galactocentric distance. Each point represents a dust cell in our simulations. They are colour-coded according to $f_{\rm young}$. The level of transparency indicates the point density. The bulge radius is indicated with a vertical red line while the vertical blue line denotes the outer truncation radius of the Ferrers-bar. The dashed black line is the running median through the data points. *Right column*: face-on view of the dust temperatures as obtained from the 3D dust cell distribution, for each galaxy. The bulge region is indicated with a solid red circle and the bar region with a dashed blue ellipse.

M 83 and M 100). At the point where the bar is truncated, this plateau is followed by a continuous decline. These results are consistent with those obtained in previous studies on the $T_{\rm dust}$ radial trends of nearby spiral galaxies (Pohlen et al. 2010; Sauvage et al. 2010; Boquien et al. 2011; Xilouris et al. 2012; Bendo et al. 2012; Galametz et al. 2012). Here we see again the possible effect of the bar to the $T_{\rm dust}$ radial profile, since the plateau (or shoulder) is seen in the bar inner region. The average $T_{\rm dust}$ in the bulge region of NGC 1365, M 83, M 95, and M 100 is warmer than the average $T_{\rm dust}$ in the bar by 25%, 22%, 28%, and 16%, respectively. We measured the global dust temperatures for NGC 1365, M 83, M 95, and M 100 to be 19.2 ± 3.8 K, 21.8 ± 3.6 K, 17.5 ± 3.0 K, and 17.6 ± 2.6 K, respectively. The average dust temperature of our galaxy sample is 19.0 ± 1.7 K. According to Nersesian et al. (2019), the average dust temperature for Sb-Sc type galaxies is 22.2 ± 3.0 K and compares fairly well with the mean dust temperature derived here for our galaxy sample.

Taking advantage of the information given by $f_{\rm young}$, it is apparent that the emission of the old stellar population is directly responsible for the high dust temperatures at the nuclear region of each galaxy. This behaviour is expected since bulges are regions of extremely high radiation density produced by old stars. For example, several studies concluded that early-type galaxies (which tend to be more concentrated than spirals and their ISRF is governed by old stellar emission) have on average warmer dust temperatures than late-type galaxies (e.g. Skibba et al. 2011; Nersesian et al. 2019). The old stellar population is also responsible for the lower dust temperatures in the bar and disc inner regions, as opposed to the higher temperatures there which are driven by star formation. In the right column of Fig. 9 we plot the dust temperature maps, to get a better visual view of the results discussed here. The bulge and the bar regions are indicated with a solid red circle and a dashed blue ellipse, respectively. Indeed, from this plot it is evident that the dust temperature is enhanced near the nucleus and along the spiral arms near star-forming regions. On the other hand, in the inter-arm and outermost regions of each galaxy, the diffuse dust is much colder. This radial trend mostly is a consequence of the diluted ISRF and possibly due to fewer young stellar populations at larger radii. The bars are not prominent in the temperature maps (with the exception of M 83). More specifically in the case of M 95, which has an inner and an outer star-forming ring with the bar acting as a bridge between them, we see that dust temperature in the inner ring ranges from 25–33 K, while the dust temperatures of the outer ring drops to 15–25 K. The old stellar population is the dominant heating agent of the diffuse dust in the outer ring of M 95, and the young stellar populations are dominating the dust-heating process in the inner ring.

6. Conclusions

We have constructed detailed 3D radiative transfer models using the state-of-the-art Monte Carlo code SKIRT, for four late-type barred spiral galaxies (NGC 1365, M 83, M 95, M 100), with the purpose of investigating the dust-heating processes and to assess the influence of the bar on the heating fraction. Our models have been validated by comparing the simulated SEDs with the observational data across the entire UV to submm wavelength range, yielding a best-fitting description of each galaxy. Here we list our main results:

- We provide global attenuation curves for NGC 1365, M 83, M 95, M 100, M 81, and M 77, and we confirm the dependence of the shape of the observed attenuation curve with the star-to-dust geometry and the level of star-formation activity. The strength of the UV bump and the slope of the attenuation curve correlate with the sSFR of a galaxy and the degree of complexity of the star-to-dust geometry.
- For the full sample, 36.5% of the bolometric luminosity is absorbed by dust. This average fraction is in line with the mean values determined by Bianchi et al. (2018), for the particular morphological group (Sb-Sc) that our galaxies fall into.
- We find that the old stellar population has a more active role in the process of dust heating. This result hints that the use

of infrared luminosity as proxy for the star-formation activity in star-forming galaxies should be used with caution. The global $f_{\rm young}$ fractions for NGC 1365, M 83, M 95, and M 100 are 68%, 64%, 47%, and 57%, respectively. We find that the old stellar population is the dominant heating source in the bulge region, while both old and young stellar populations are equally responsible for the dust heating in the bar region.

– We confirm a strong link between $f_{\rm young}$ and the sSFR which was previously reported in the radiative transfer model analysis of M 51 (De Looze et al. 2014), M 31 (Viaene et al. 2017), and M 81 (Verstocken et al. 2020), as well as in studies of Nersesian et al. (2019) for the DustPedia galaxy sample and Leja et al. (2019) for the 3D-HST galaxy sample, and provide a relation to calibrate the contribution of the old stellar population to dust heating in global SED modelling.
– We confirm that the central regions and the two diametrically opposed ends of the bar are places of enhanced star formation and show that the bar in those galaxies affects the radial profiles of the $f_{\rm young}$ and dust temperature. On average, the diffuse dust temperatures at the central regions of galaxies are warmer than those at the bar regions, while $T_{\rm dust}$ decreases towards the outer parts of galaxies. The old stellar population is exclusively responsible for the warmer $T_{\rm dust}$ at the bulge and the colder $T_{\rm dust}$ across the galactic disc of galaxies. The young stellar populations are responsible for the warmer $T_{\rm dust}$ in the spiral arms and near the star-forming dust clouds. The average dust temperature of our galaxy sample is 19.0 ± 1.7 K and is comparable to the mean values derived by Nersesian et al. (2019), for the particular morphological group (Sb-Sc) that our galaxies fall into.

The full description of our framework and the results of the radiation transfer modelling of M 81 are presented in Verstocken et al. (2020), while the modelling results of a galaxy with the addition of an AGN component, NGC 1068 (M 77) will be presented in Viaene et al. (2020). The continuation of the 3D radiation transfer modelling in a statistically significant sample of nearby spatially resolved galaxies, which have been modelled in a homogeneous way, will allow us to better understand the scatter in the sSFR–$f_{\rm young}$ relation but also to investigate the properties of dust (e.g. composition, size distribution, etc.) and possible variations in the dust-heating processes among different galaxy types in the local Universe.

Acknowledgements. We thank the referee, Adolf Witt, for his helpful comments and suggestions. DustPedia is a collaborative focused research project supported by the European Union under the Seventh Framework Programme (2007-2013) call (proposal no. 606847). The participating institutions are: Cardiff University, UK; National Observatory of Athens, Greece; Ghent University, Belgium; Université Paris Sud, France; National Institute for Astrophysics, Italy and CEA, France. AN gratefully acknowledges the financial support from Greece and the European Union (European Social Fund- ESF) through the Operational Programme “Human Resources Development, Education and Lifelong Learning” in the context of the project “Strengthening Human Resources Research Potential via Doctorate Research” (MIS-5000432), implemented by the State Scholarships Foundation (IKY). This research made use of Astropy, (`http://www.astropy.org`) a community-developed core Python package for Astronomy (Astropy Collaboration 2013, 2018). This research has made use of the NASA/IPAC Infrared Science Archive (IRSA; `http://irsa.ipac.caltech.edu`), and the NASA/IPAC Extragalactic Database (NED; `https://ned.ipac.caltech.edu`), both of which are operated by the Jet Propulsion Laboratory, California Institute of Technology, under contract with the National Aeronautics and Space Administration. The computational resources (Stevin Supercomputer Infrastructure) and services used in this work were provided by the VSC (Flemish Supercomputer Center), funded by Ghent University, FWO and the Flemish Government – department EWI.

References

Astropy Collaboration (Robitaille, T. P., et al.) 2013, A&A, 558, A33
Astropy Collaboration (Price-Whelan, A. M., et al.) 2018, AJ, 156, 123
Baes, M., & Camps, P. 2015, Astron. Comput., 12, 33
Baes, M., Fritz, J., Gadotti, D. A., et al. 2010, A&A, 518, L39
Baes, M., Verstappen, J., De Looze, I., et al. 2011, ApJS, 196, 22
Bendo, G. J., Wilson, C. D., Pohlen, M., et al. 2010, A&A, 518, L65
Bendo, G. J., Boselli, A., Dariush, A., et al. 2012, MNRAS, 419, 1833
Bendo, G. J., Baes, M., Bianchi, S., et al. 2015, MNRAS, 448, 135
Bianchi, S. 2007, A&A, 471, 765
Bianchi, S., De Vis, P., Viaene, S., et al. 2018, A&A, 620, A112
Boquien, M., Calzetti, D., Combes, F., et al. 2011, AJ, 142, 111
Boquien, M., Burgarella, D., Roehlly, Y., et al. 2019, A&A, 622, A103
Bruzual, G., & Charlot, S. 2003, MNRAS, 344, 1000
Buat, V., Boquien, M., Małek, K., et al. 2018, A&A, 619, A135
Buat, V., Corre, D., Boquien, M., & Malek, K. 2019, ArXiv e-prints [arXiv:1902.09435]
Calzetti, D., Armus, L., Bohlin, R. C., et al. 2000, ApJ, 533, 682
Calzetti, D., Kennicutt, R. C., Engelbracht, C. W., et al. 2007, ApJ, 666, 870
Calzetti, D., Wu, S.-Y., Hong, S., et al. 2010, ApJ, 714, 1256
Camps, P., & Baes, M. 2015, Astron. Comput., 9, 20
Camps, P., Baes, M., & Saftly, W. 2013, A&A, 560, A35
Cardelli, J. A., Clayton, G. C., & Mathis, J. S. 1989, ApJ, 345, 245
Casasola, V., Hunt, L. K., Combes, F., García-Burillo, S., & Neri, R. 2011, A&A, 527, A92
Casasola, V., Cassarà, L. P., Bianchi, S., et al. 2017, A&A, 605, A18
Chabrier, G. 2003, PASP, 115, 763
Chang, Y.-Y., van der Wel, A., da Cunha, E., & Rix, H.-W. 2015, ApJS, 219, 8
Charlot, S., & Fall, S. M. 2000, ApJ, 539, 718
Ciesla, L., Boquien, M., Boselli, A., et al. 2014, A&A, 565, A128
Clark, C. J. R., Verstocken, S., Bianchi, S., et al. 2018, A&A, 609, A37
Combes, F., García-Burillo, S., Casasola, V., et al. 2013, A&A, 558, A124
Combes, F., García-Burillo, S., Casasola, V., et al. 2014, A&A, 565, A97
Cortese, L., Boselli, A., Franzetti, P., et al. 2008, MNRAS, 386, 1157
Cutri, R. M., Skrutskie, M. F., van Dyk, S., et al. 2003, VizieR Online Data Catalog: II/246
da Cunha, E., Charlot, S., & Elbaz, D. 2008, MNRAS, 388, 1595
Davies, L. J. M., Driver, S. P., Robotham, A. S. G., et al. 2016, MNRAS, 461, 458
Davies, J. I., Baes, M., Bianchi, S., et al. 2017, PASP, 129, 044102
De Geyter, G., Baes, M., Camps, P., et al. 2014, MNRAS, 441, 869
De Geyter, G., Baes, M., De Looze, I., et al. 2015, MNRAS, 451, 1728
De Looze, I., Baes, M., Fritz, J., & Verstappen, J. 2012a, MNRAS, 419, 895
De Looze, I., Baes, M., Bendo, G. J., et al. 2012b, MNRAS, 427, 2797
De Looze, I., Fritz, J., Baes, M., et al. 2014, A&A, 571, A69
de Vaucouleurs, G., de Vaucouleurs, A., Corwin, H. G., et al. 1995, VizieR Online Data Catalog: VII/155
De Vis, P., Jones, A., Viaene, S., et al. 2019, A&A, 623, A5
Eisenstein, D. J., Weinberg, D. H., Agol, E., et al. 2011, AJ, 142, 72
Fazeli, N., Busch, G., Valencia, S. M., et al. 2019, A&A, 622, A128
Fazio, G. G., Hora, J. L., Allen, L. E., et al. 2004, ApJS, 154, 10
Fitzpatrick, E. L., & Massa, D. 2007, ApJ, 663, 320
Fitzpatrick, E. L., & Massa, D. 2009, ApJ, 699, 1209
Galametz, M., Kennicutt, R. C., Albrecht, M., et al. 2012, MNRAS, 425, 763
Galametz, M., Kennicutt, R. C., Calzetti, D., et al. 2013, MNRAS, 431, 1956
Galliano, F., Galametz, M., & Jones, A. P. 2018, ARA&A, 56, 673
George, K., Joseph, P., Mondal, C., et al. 2019, A&A, 621, L4
Gordon, K. D., Clayton, G. C., Misselt, K. A., Landolt, A. U., & Wolff, M. J. 2003, ApJ, 594, 279
Granato, G. L., Lacey, C. G., Silva, L., et al. 2000, ApJ, 542, 710
Griffin, M. J., Abergel, A., Abreu, A., et al. 2010, A&A, 518, L3
Groves, B., Dopita, M. A., Sutherland, R. S., et al. 2008, ApJS, 176, 438
Hinz, J. L., Rieke, G. H., Gordon, K. D., et al. 2004, ApJS, 154, 259
Ho, L. C., Filippenko, A. V., & Sargent, W. L. W. 1997, ApJS, 112, 315
Indebetouw, R., Whitney, B. A., Johnson, K. E., & Wood, K. 2006, ApJ, 636, 362
James, P. A., & Percival, S. M. 2015, MNRAS, 450, 3503
James, P. A., & Percival, S. M. 2016, MNRAS, 457, 917
James, P. A., Bretherton, C. F., & Knapen, J. H. 2009, A&A, 501, 207
Jones, A. P., Fanciullo, L., Köhler, M., et al. 2013, A&A, 558, A62
Jones, A. P., Köhler, M., Ysard, N., Bocchio, M., & Verstraete, L. 2017, A&A, 602, A46
Kennicutt, Jr., R. C. 1998, ARA&A, 36, 189
Kennicutt, R. C., & Evans, N. J. 2012, ARA&A, 50, 531
Kennicutt, Jr., R. C., Hao, C.-N., Calzetti, D., et al. 2009, ApJ, 703, 1672
Knapen, J. H., Pérez-Ramírez, D., & Laine, S. 2002, MNRAS, 337, 808

Knapen, J. H., Sharp, R. G., Ryder, S. D., et al. 2010, MNRAS, 408, 797
Köhler, M., Jones, A., & Ysard, N. 2014, A&A, 565, L9
Kriek, M., & Conroy, C. 2013, ApJ, 775, L16
Lauberts, A., & Valentijn, E. A. 1989, The Messenger, 56, 31
Leja, J., Johnson, B. D., Conroy, C., van Dokkum, P. G., & Byler, N. 2017, ApJ, 837, 170
Leja, J., Johnson, B. D., Conroy, C., et al. 2019, ApJ, 877, 140
Lenz, D., Hensley, B. S., & Doré, O. 2017, ApJ, 846, 38
Lindblad, P. O. 1999, A&ARv, 9, 221
Lindblad, P. O., Hjelm, M., Hoegbom, J., et al. 1996, A&AS, 120, 403
Liszt, H. 2014a, ApJ, 780, 10
Liszt, H. 2014b, ApJ, 783, 17
Makarov, D., Prugniel, P., Terekhova, N., Courtois, H., & Vauglin, I. 2014, A&A, 570, A13
Mathis, J. S., Mezger, P. G., & Panagia, N. 1983, A&A, 128, 212
Mazzalay, X., Saglia, R. P., Erwin, P., et al. 2013, MNRAS, 428, 2389
Morrissey, P., Conrow, T., Barlow, T. A., et al. 2007, ApJS, 173, 682
Mosenkov, A. V., Allaert, F., Baes, M., et al. 2016, A&A, 592, A71
Mosenkov, A. V., Allaert, F., Baes, M., et al. 2018, A&A, 616, A120
Mosenkov, A. V., Baes, M., Bianchi, S., et al. 2019, A&A, 622, A132
Narayanan, D., Conroy, C., Davé, R., Johnson, B. D., & Popping, G. 2018, ApJ, 869, 70
Nersesian, A., Xilouris, E. M., Bianchi, S., et al. 2019, A&A, 624, A80
Nguyen, H., Dawson, J. R., Miville-Deschênes, M.-A., et al. 2018, ApJ, 862, 49
Noll, S., Burgarella, D., Giovannoli, E., et al. 2009, A&A, 507, 1793
Oliver, S., Frost, M., Farrah, D., et al. 2010, MNRAS, 405, 2279
Peng, Y.-J., Lilly, S. J., Kovač, K., et al. 2010, ApJ, 721, 193
Pilbratt, G. L., Riedinger, J. R., Passvogel, T., et al. 2010, A&A, 518, L1
Planck Collaboration I. 2011, A&A, 536, A1
Planck Collaboration XXIV. 2011, A&A, 536, A24
Poglitsch, A., Waelkens, C., Geis, N., et al. 2010, A&A, 518, L2
Pohlen, M., Cortese, L., Smith, M. W. L., et al. 2010, A&A, 518, L72
Popescu, C. C., & Tuffs, R. J. 2002, in Reviews in Modern Astronomy, ed. R. E. Schielicke, 15, 239
Reach, W. T., Heiles, C., & Bernard, J.-P. 2015, ApJ, 811, 118
Reach, W. T., Heiles, C., & Bernard, J.-P. 2017a, ApJ, 834, 63
Reach, W. T., Bernard, J.-P., Jarrett, T. H., & Heiles, C. 2017b, ApJ, 851, 119
Reddy, N. A., Kriek, M., Shapley, A. E., et al. 2015, ApJ, 806, 259
Saftly, W., Camps, P., Baes, M., et al. 2013, A&A, 554, A10
Saftly, W., Baes, M., & Camps, P. 2014, A&A, 561, A77
Saftly, W., Baes, M., De Geyter, G., et al. 2015, A&A, 576, A31
Salo, H., Laurikainen, E., Laine, J., et al. 2015, ApJS, 219, 4
Sauvage, M., Sacchi, N., Bendo, G. J., et al. 2010, A&A, 518, L64
Sheth, K., Regan, M., Hinz, J. L., et al. 2010, PASP, 122, 1397
Silva, L., Granato, G. L., Bressan, A., & Danese, L. 1998, ApJ, 509, 103
Skibba, R. A., Engelbracht, C. W., Dale, D., et al. 2011, ApJ, 738, 89
Skrutskie, M. F., Cutri, R. M., Stiening, R., et al. 2006, AJ, 131, 1163
Smith, M. W. L., Eales, S. A., Gomez, H. L., et al. 2012, ApJ, 756, 40
Soifer, B. T., & Neugebauer, G. 1991, AJ, 101, 354
Telesco, C. M., & Harper, D. A. 1980, ApJ, 235, 392
Teuben, P. J., Sanders, R. H., Atherton, P. D., & van Albada, G. D. 1986, MNRAS, 221, 1
Turner, J. L., Ho, P. T. P., & Beck, S. 1987, ApJ, 313, 644
Városi, F., & Dwek, E. 1999, ApJ, 523, 265
Véron-Cetty, M.-P., & Véron, P. 2006, A&A, 455, 773
Verstocken, S., Van De Putte, D., Camps, P., & Baes, M. 2017, Astron. Comput., 20, 16
Verstocken, S., Nersesian, A., Baes, M., et al. 2020, A&A, 637, A24
Viaene, S., Baes, M., Bendo, G., et al. 2016, A&A, 586, A13
Viaene, S., Baes, M., Tamm, A., et al. 2017, A&A, 599, A64
Viaene, S., Nersesian, A., Fritz, J., et al. 2020, A&A submitted
Werner, M. W., Roellig, T. L., Low, F. J., et al. 2004, ApJS, 154, 1
Whelan, D. G., Johnson, K. E., Whitney, B. A., Indebetouw, R., & Wood, K. 2011, ApJ, 729, 111
Whitaker, K. E., Bezanson, R., van Dokkum, P. G., et al. 2017, ApJ, 838, 19
Williams, T. G., Baes, M., De Looze, I., et al. 2019, MNRAS, 487, 2753
Witt, A. N., & Gordon, K. D. 1996, ApJ, 463, 681
Witt, A. N., & Gordon, K. D. 2000, ApJ, 528, 799
Wozniak, H. 2007, A&A, 465, L1
Wright, E. L., Eisenhardt, P. R. M., Mainzer, A. K., et al. 2010, AJ, 140, 1868
Xilouris, E. M., Byun, Y. I., Kylafis, N. D., Paleologou, E. V., & Papamastorakis, J. 1999, A&A, 344, 868
Xilouris, E. M., Tabatabaei, F. S., Boquien, M., et al. 2012, A&A, 543, A74
York, D. G., Adelman, J., Anderson, Jr., J. E., et al. 2000, AJ, 120, 1579
Ysard, N., Köhler, M., Jones, A., et al. 2015, A&A, 577, A110
Zabel, N., Davis, T. A., Smith, M. W. L., et al. 2019, MNRAS, 483, 2251

Appendix A: Global photometry

Table A.1. Integrated flux densities for our galaxy sample in this paper, listed by increasing central wavelength.

Instrument	Band	$\lambda_{\rm eff}$ [μm]	NGC 1365 Flux density [Jy]	M 83 Flux density [Jy]	M 95 Flux density [Jy]	M 100 Flux density [Jy]
GALEX	FUV	0.154	0.043 ± 0.002	0.287 ± 0.013	0.016 ± 0.001	0.031 ± 0.002
GALEX	NUV	0.227	0.061 ± 0.002	0.470 ± 0.013	0.027 ± 0.001	0.054 ± 0.002
SDSS	u	0.359	–	–	0.081 ± 0.001	0.202 ± 0.003
SDSS	g	0.464	–	–	0.340 ± 0.003	0.498 ± 0.004
SDSS/Other	$r/R_{\rm C}$	0.612	0.907 ± 0.007	5.455 ± 0.044	0.632 ± 0.005	0.815 ± 0.006
SDSS	i	0.744	–	–	0.896 ± 0.006	1.134 ± 0.008
SDSS	z	0.890	–	–	1.007 ± 0.008	1.237 ± 0.010
2MASS	J	1.235	1.796 ± 0.050	9.818 ± 0.275	1.470 ± 0.041	1.681 ± 0.047
2MASS	H	1.662	1.710 ± 0.050	11.870 ± 0.332	1.946 ± 0.054	2.117 ± 0.059
2MASS	Ks	2.159	1.698 ± 0.050	8.350 ± 0.234	1.573 ± 0.044	1.430 ± 0.040
WISE	W1	3.352	1.214 ± 0.035	6.113 ± 0.180	0.814 ± 0.024	0.922 ± 0.027
IRAC	I1	3.508	1.170 ± 0.035	6.295 ± 0.190	0.805 ± 0.024	0.967 ± 0.030
IRAC	I2	4.437	0.884 ± 0.027	4.124 ± 0.124	0.498 ± 0.015	0.628 ± 0.020
WISE	W2	4.603	0.885 ± 0.030	3.818 ± 0.130	0.439 ± 0.015	0.519 ± 0.018
IRAC	I3	5.628	2.190 ± 0.066	12.400 ± 0.370	0.820 ± 0.025	1.314 ± 0.040
IRAC	I4	7.589	5.210 ± 0.156	30.051 ± 0.901	1.612 ± 0.048	3.318 ± 0.010
WISE	W3	11.56	4.164 ± 0.192	21.105 ± 0.971	1.080 ± 0.050	2.452 ± 0.113
WISE	W4	22.09	12.472 ± 0.698	45.804 ± 2.565	2.690 ± 0.151	3.690 ± 0.207
MIPS	24	23.21	8.853 ± 0.443	39.885 ± 1.994	2.387 ± 0.119	3.318 ± 0.166
MIPS	70	68.44	–	306.368 ± 30.640	–	35.647 ± 3.565
PACS	70	68.92	138.496 ± 9.695	448.555 ± 31.398	25.907 ± 1.813	42.932 ± 3.005
PACS	100	100.8	214.973 ± 15.048	–	49.566 ± 3.470	87.256 ± 6.108
MIPS	160	152.6	–	756.137 ± 90.740	–	117.714 ± 14.126
PACS	160	153.9	204.472 ± 14.313	834.000 ± 58.380	54.741 ± 3.832	115.215 ± 8.065
SPIRE	PSW	247.1	99.620 ± 5.480	371.240 ± 20.420	29.693 ± 1.633	63.481 ± 3.491
SPIRE	PMW	346.7	43.280 ± 2.380	148.972 ± 8.194	13.183 ± 0.725	26.801 ± 1.474
HFI	**857**	349.9	37.410 ± 2.390	134.040 ± 8.578	9.535 ± 0.610	16.454 ± 1.053
SPIRE	PLW	496.1	15.085 ± 0.830	50.356 ± 2.770	4.804 ± 0.264	9.054 ± 0.498
HFI	**545**	550.1	11.470 ± 0.700	34.851 ± 2.126	2.544 ± 0.155	4.753 ± 0.300
HFI	**353**	849.3	2.424 ± 0.020	3.900 ± 0.030	0.766 ± 0.006	1.056 ± 0.008

Notes. The bands not used in our modelling are indicated in boldface.

Table A.1 summarises the final aperture photometry flux densities extracted from the image data, used for the radiative transfer modelling. The bands that were not used in our modelling are indicated in boldface.

Appendix B: Image comparison

Figures B.1–B.3 show the observational, model, and residual images for 6 wavebands that were fitted with SKIRT. Residuals are calculated as the relative difference between the modelled and the observed flux densities (Eq. (1)). Overall, the observations are fitted quite well with absolute residuals within 50% in all three galaxies. The largest discrepancies can be seen for NGC 1365, for the IRAC 3.6 μm and MIPS 24 μm wavebands. The model overestimates the observations with absolute residuals higher than 50%, especially for MIPS 24 μm, where the model overestimates the flux densities up to 100%, with the extremely bright AGN in the centre as a possible cause. In the fourth panel of Fig. 1a (young ionising stellar disc), an Airy ring effect is still visible, despite our efforts to subtract the AGN emission (PSF) from the original image by employing 2D decomposition with GALFIT (Peng et al. 2010). To be more specific, since AGN is a point source we convolved it with the PSF for the MIPS 24 μm image. We assumed a model for that galaxy that includes an AGN, a Sérsic bulge, a Ferrers bar and an exponential disc, and then we subtracted the modelled AGN from the original image. Nevertheless, the residuals of the remaining wavebands and galaxies are still more or less within 50%, and with very narrow residual distributions, indicating that our simulations are accurate representations of the observed data. A detailed explanation of the cause of several residuals in these maps is given in Sect. 4.2.